https://doi.org/10.5194/egusphere-2026-4121
Preprint. Discussion started: 5 August 2026

Seasonal Evolution of Thermal, Dynamic, and Material Boundary Layers and their impacts on air pollution in the Megacity Beijing

Jinyuan Xin[1,2]*, Masroor Ahmed[1,2], Yulong Tan[1,2], Guiqian Tang[1,2] Xinbing Ren[1,3], Dandan Zhao[1,3], Luoqi Yang[1,2], Nanfangyu Qiu[1], Junji Cao[1,2], Zhang Lei[4], Yongjing Ma[1,2]

[1] State Key Laboratory of Atmospheric Environment and Extreme Meteorology, Institute of Atmospheric Physics, Chinese Academy of Sciences, Beijing, 100029, China.
[2] University of Chinese Academy of Sciences, Beijing, 100049, China
[3] College of Aviation Meteorology, Civil Aviation Flight University of China, Chengdu, 641419, China.
[4] China Meteorological Administration Training Center, 100081, Beijing, China

* *Correspondence to*: Jinyuan Xin (xjy@mail.iap.ac.cn)

Abstract. Urban planetary boundary layer height (PBLH) regulates the exchange of heat, momentum, moisture, aerosols, and pollutants between the surface and free troposphere, yet a single PBLH estimate cannot represent the multiple physical interfaces controlling turbulent mixing in complex megacities. This study investigates the seasonal co-evolution of thermal, dynamic, and material PBLHs in Beijing using the parcel, Richardson number (Ri), and gradient methods. Dynamic PBLH dominated during winter, with a mean of 828 m exceeding thermal (666 m) and material (625 m) PBLHs. In spring, material (918 m) and dynamic (871) PBLHs also exceeded the thermal PBLH (657 m). Summer exhibited the deepest daytime PBLH growth, with median peak thermal, dynamic and material PBLHs of 1397 m, 1402 m, and 1464 m, respectively. Autumn showed a transition regime, with mean thermal (685 m), dynamic (591 m) and material (709 m) PBLHs. In winter, pollutant concentrations were negatively correlated with dynamic PBLH (ρ= -0.47 to -0.74). Weak thermal buoyancy suppressed vertical mixing and restricted the upward transport of pollutant into the free atmosphere, favouring local pollution accumulation except during strong cold-air advection. In summer and autumn, thermal and material PBLHs exceeded the dynamic PBLH. Strong thermal buoyancy lifted particulate matter and other primary pollutants above the dynamic PBL top, facilitating long range dispersion. In contrast, ozone exhibited positive correlations with all PBLH metrics, consistent with active photochemical production and vigorous convective mixing. Collectively, these results demonstrate that adopting multiple definitions of BLH provides a comprehensive understanding of the processes controlling atmospheric pollution.

https://doi.org/10.5194/egusphere-2026-4121
Preprint. Discussion started: 5 August 2026

Graphical Abstract

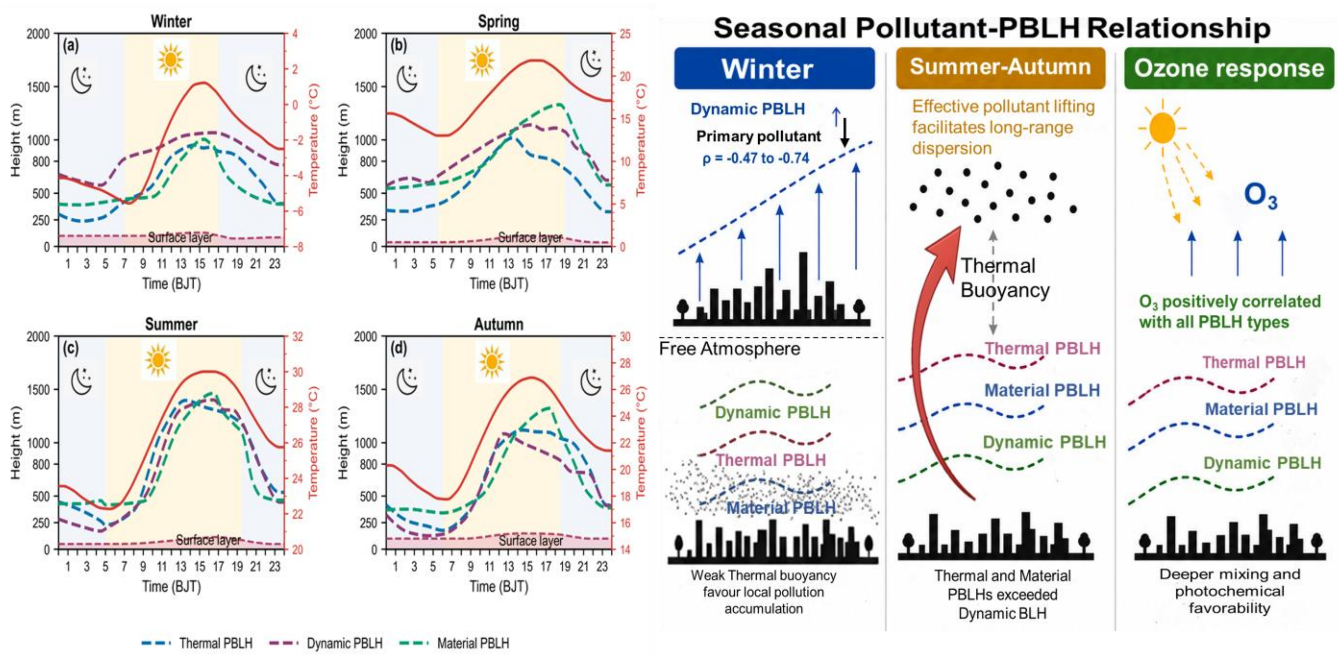

1 Introduction

The atmospheric planetary boundary layer (PBL), which is the lowest layer of Earth's atmosphere, is responsible for regulating the exchange of heat, momentum, moisture, and pollutants between the surface and the free troposphere, thereby having a profound effect on near-surface meteorology and air quality in urban areas (Oke et al., 2017; Zhao et al., 2020; Sun et al., 2021; Yan et al., 2023; Ma et al., 2024; Yang et al., 2025). In urban area and their surroundings, the variations in surface characteristics and mesoscale circulations introduce additional challenges to understanding the structure of the PBL, suggesting that a single estimate of PBLH does not accurately represent the full state of turbulent exchange (Bou-Zeid et al., 2020; Tan et al., 2025). More broadly, boundary layer meteorology has evolved from being centered on near-surface observations to a field that covers a diverse ABL regimes across a wide range of environments (LeMone et al., 2019).

A variety of approaches have been developed to determine the PBL height, including diagnostic formulas and forecasting models, satellite-based remote sensing inversion methods, and analytical approaches that focus on specific atmospheric variables. Among these, the most widely used rely on vertical profiles of temperature, humidity, wind, turbulence, aerosols, or atmospheric composition. However, these methods may not represent the same physical interface; therefore, it is important to distinguish between them (Collaud et al., 2014; Shi et al., 2020; Kotthaus et al., 2023). The thermal PBL can be classified into convective and stable regimes. For convective conditions, the thermodynamic BL is often defined by the parcel method, which locates the CBL top where a surface parcel lifted adiabatically reaches the same virtual potential temperature as the environment, whereas in the stable BL it is defined by the top of the near-surface inversion layer (Seidel et al., 2010; Collaud et al., 2014; Du et al., 2013; Zhou et al., 2025). The potential temperature method is widely used to determine the height of

https://doi.org/10.5194/egusphere-2026-4121
Preprint. Discussion started: 5 August 2026

thermal BL notably under the effect of thermal motions (Liu and Liang, 2010). Material PBLH can be retrieved from aerosol lidar or ceilometer backscatter profiles using gradient (Sicard et al., 2006), threshold (Strawbridge and Snyder, 2004), and wavelet-based methods (Brooks, 2003), even though these techniques can be considerably influenced by high humidity, low clouds, fog, and complex cloud formation (Emeis et al., 2008; Haeffelin et al., 2012; Pal et al., 2013). The dynamic PBLH can be determined using turbulence metrics for Doppler wind lidar, including vertical velocity variance, dissipation measures and spectral characteristics. These parameters reflect the strength of turbulence and the vertical extent of turbulent mixing (Tucker et al., 2009; Su et al., 2024; Xian et al., 2024). However, these retrievals are subject to the influence of empirical thresholds, the quality of the signal, and discrepancies in sampling between instruments, which may complicate the understanding of dynamic boundary layer structure under different weather regimes (Barlow et al., 2011; Schween et al., 2014).

Previous studies have analyzed boundary layer evolution from several perspectives. Long-term monitoring studies have documented climatological and diurnal variations of mixing layer height (MLH) between urban and suburban areas (Zhu et al., 2018; Wang et al., 2021). Other studies have emphasized spatial contrasts, showing clear differences in boundary layer evolution between urban and suburban areas (Wang et al., 2020). In Beijing, Jiang et al. (2021b) compared the thermodynamic and material PBLHs in different seasons and found considerable differences between them, indicating that boundary layer definitions are not identical because they are based on different stratification methods. Observation from towers and Doppler lidar (Wang et al., 2024) have further shown that urban boundary layer structure in Beijing is mainly active for most of the daytime hours, whereas strong stable regimes tend to occur more often in the winter and autumn seasons, particularly in the transition periods from night to morning. Dai et al. (2025) reported elevated thermodynamic and material PBLHs during heatwaves in Beijing however, material PBLH is usually higher than thermodynamic PBLH and the variations between them are significantly affected by temperature, humidity, wind direction, wind speed and ozone conditions. Tan et al. (2025) highlighted in their recent study that, in complex terrains, thermal, dynamic, and material PBLHs can vary considerably and motivate further studies across diverse geographical and seasonal analysis to improve the existing conceptual framework.

Despite the extensive research on PBLH from various observational perspectives, most of the existing literature predominantly emphasizes a single PBLH, event types, or specific observational settings and very few studies have examined multi PBLH frameworks. As a result, the co-evolution of thermal, dynamic, and material PBLHs, as well as their similarities and differences across seasons and between daytime and nighttime conditions, particularly in complex urban environments is still not well understood. To address these gaps, the proposed study retrieved thermal, dynamic and material PBLHs from microwave radiometer, Doppler wind lidar, and ceilometer in Beijing. The objectives of the study are: (1) to evaluate the characteristic differences of thermal, dynamic, and material boundary layer heights in different seasons and day-night conditions; (2) to assess how meteorological forcing and air pollutants modulate these differences. These findings aim to provide a comprehensive urban, geographical and seasonal analysis that contributes to the improvement of the existing PBL framework.

2 Materials and Methods

2.1 Introduction of Study Area and Instruments

https://doi.org/10.5194/egusphere-2026-4121
Preprint. Discussion started: 5 August 2026

The ceilometer, microwave radiometer, and wind lidar were deployed in the courtyard of the Institute of Atmospheric Physics, Chinese Academy of Sciences, Beijing. The observation location is situated at 39.6°N latitude and 116.2°E longitude (Figure 1). The microwave radiometer provides vertical observations with a resolution of 10–30 m from the surface to 0.5 km, 40–90 m from 0.5 to 2.5 km, and 100–200 m from 2 to 10 km. A total of 93 vertical layers are sampled, with data recorded at a temporal resolution of 1 second. The Doppler wind lidar operated in Doppler Beam Swinging mode, recording wind profiles every 5 seconds. Data with a carrier-to-noise ratio below -26 dBZ were discarded. Quality control eliminated invalid entries such as zero, NaN, and flagged 999 values. The Vaisala CL31 cloud altimeter has a vertical resolution of 10 meter and a maximum detection range of 7.7 km.

The RPG-HATPRO-G5 radiometer provides temperature (RMS error: 0.25–1.00 K), relative humidity (5%), and absolute humidity (≤0.3 g/m³ bias) profiles. Wind speed profiles from the WindCube 100S have 0.5 m/s accuracy. For PBL detection, Vaisala's BL-View software identifies up to three PBL heights, using the largest negative gradients in backscatter profiles. Furthermore, previous studies (Dai et al., 2020; Yang et al., 2024) have revealed that both microwave radiometer and wind lidar exhibit a strong correlation with the measurement taken from the 325-m meteorological tower. Thus, the vertical profiles obtained from ground-based remote sensing instruments were validated against tower-based observations, demonstrating high reliability, low measurement uncertainty, and supporting their use in interpreting PBL variability.

2.2 Thermal PBL Height Calculation

The specific humidity (q) and virtual potential temperature (θ_v) at each level can be derived from Equation 1 and 2.

$$q = \frac{0.622 e_s \times RH\%}{P - 0.378 e_s \times RH\%} \tag{1}$$

$$\theta_v = T \left(\frac{P_0}{P}\right)^{R/C_P} (1 + 0.608q) \tag{2}$$

where P, P_0, es and T signify the atmospheric pressure, sea-level pressure, saturated water vapor pressure, and temperature at each level, respectively. The Goff-Gratch formula (Goff and Gratch, 1946) is employed to calculate e_s. The ideal gas constant is denoted by R, while C_p refers to the specific heat capacity maintained at constant pressure. In order to address the possible accumulation of water vapor in the lower atmosphere, θ_v is employed to prevent potential biases associated with water vapor.

Holzworth (1964), Siedel et al. (2010), Collaud Coen et al. (2014), and Ma et al. (2024) describe the parcel method for calculating the height of the thermal PBL. The steps for the calculation are as follows.

1. Determine whether the requirement for the parcel method is satisfied: if a particular height exists such as $\theta(z)<\theta 0$, this signifies the depth of the CBL in a convective state, specifically,

$$\theta_v(z) = \theta_v(0) \tag{3}$$

2. The height that fulfils this criterion is termed the thermal PBL during the daytime. If the criteria for the parcel method are not satisfied, it is regarded as stable. In this scenario, the corresponding PBL is the top of SBL, characterized by a decreasing derivative of $\theta(z)$ (Collaud Coen et al., 2014; Moreira et al., 2020). In cases where the minimum value of $\partial\theta v/\partial z$ is equal to or

https://doi.org/10.5194/egusphere-2026-4121
Preprint. Discussion started: 5 August 2026

exceeds zero, the altitude at which this minimum is identified (i.e., argmin ($\frac{\partial\theta_v}{\partial z}$)) is referred to as the top of the SBL. Newton-Raphson method is used to perform this iterative calculation. Traditional moving average methods often produce a lag that changes with the size of the selected sliding window. To address this problem, a centered moving average strategy is applied to smooth the data. This method is specifically executed through the rolling attribute of the pandas DataFrame, with a window size of 7 (reflecting 7 observations) and centre = True parameter to preserve symmetry around each data point (McKinney, 2010).

2.3 Dynamic BL Height Calculation

The height of dynamic PBL indicates the vertical range of atmospheric flow that can show either laminar or turbulent behaviour. Thus, the bulk Richardson number (Ri) is an important parameter for determining whether the boundary layer is mainly in a laminar or turbulent state. In this study, finite-difference transformations are utilized to derive the bulk Ri following the approach outlined by Mauritsen and Svensson (2007) and Tan et al. (2025), because it is well suited for use with altitude levels obtained from instruments.

$$\mathrm{Ri} \approx \frac{2g}{\theta_{va} + \theta_{vb}} \frac{(\theta_{va} - \theta_{vb})\,(z_a - z_b)}{(U_a + U_b)^2 + (V_a - V_b)^2}\ (\mathrm{a} < \mathrm{b}) \tag{4}$$

where a and b denote the altitudes obtained from microwave radiometer and wind lidar observations respectively.

Based on the criteria for assessing dynamic stability as defined by Ri (Stull, 1988, 2017; Woods, 1969), the critical values R_c = 0.25 and R_T = 1 are adopted. The range between these critical values is viewed as the transitional interval, which is determined by the historical flow state of the boundary layer.

$$R_i < R_c \text{ , be Turbulent}$$

(5)

$$\mathrm{Ri} < \mathrm{RT}\text{, Be laminar on the condition of SBL}$$

2.4 Material PBLH Height Calculation

The Vaisala CL31 ceilometer designed chiefly for the measurement of cloud base height however, it also offers backscatter profiles and is extensively utilized in studies of the boundary layer research (Jin et al., 2015; Mues et al., 2017; Zhu et al., 2018; Zhao et al., 2020; Jiang et al., 2021b). As a result of achieving a full overlap through the use of the same telescope for both transmitting and receiving, backscatter can be used from the first range (Münkel et al., 2007). The operating principle is based on the identification of short pulses that are transmitted by the ceilometer through the atmosphere and reflected back by the cloud's lower boundary. The resolution for range detection of the backscatter is 10 m and the backscatter profile can extend up to 7.7 kilometres. Assuming that the mixed layer has a relatively uniform aerosol concentration that is significantly higher than that of the air above (Steyn et al., 1999), PBLHs are calculated using BL-VIEW software developed by the Vaisala Corporation, which is based on the minima of the local backscatter gradient. Various thresholds are implemented to separate

https://doi.org/10.5194/egusphere-2026-4121
Preprint. Discussion started: 5 August 2026

clouds, precipitation, and fog from aerosols (Knepp et al., 2017). Backscatter is processed using temporal and spatial sliding averages to remove unnecessary fluctuations, except for those related to clouds and precipitation. Height averaging intervals extend from 80 m in the lowest 100 m above ground to 360 m at altitudes of 2000 m and higher. The PBL-VIEW software simultaneously produces three potential PBLH values at a temporal resolution of 10 minutes using the first three largest negative gradients in the backscatter coefficient profile. At night the aerosols boundary layer is defined by multiple layers. Two distinct layers emerge, representing the Stable Boundary Layer (SBL) and the Residual Layer (RL) at most nights. The height of lower layer (SBL) is chosen for comparison with the PBLH derived from MWR.

2.5. Air pollutants data

Hourly concentration of PM_{10}, $PM_{2.5}$, NO_2, SO_2, CO, and O_3 were collected from the China National Environmental Monitoring Centre (CNEMC) https://www.cnemc.cn/en/ last access April 15 2026. To represent the urban area of Beijing, eight national air quality monitoring stations were selected. For each pollutant, the hourly concentration from all available stations were averaged to generate a representative hourly urban pollution dataset for subsequent analysis.

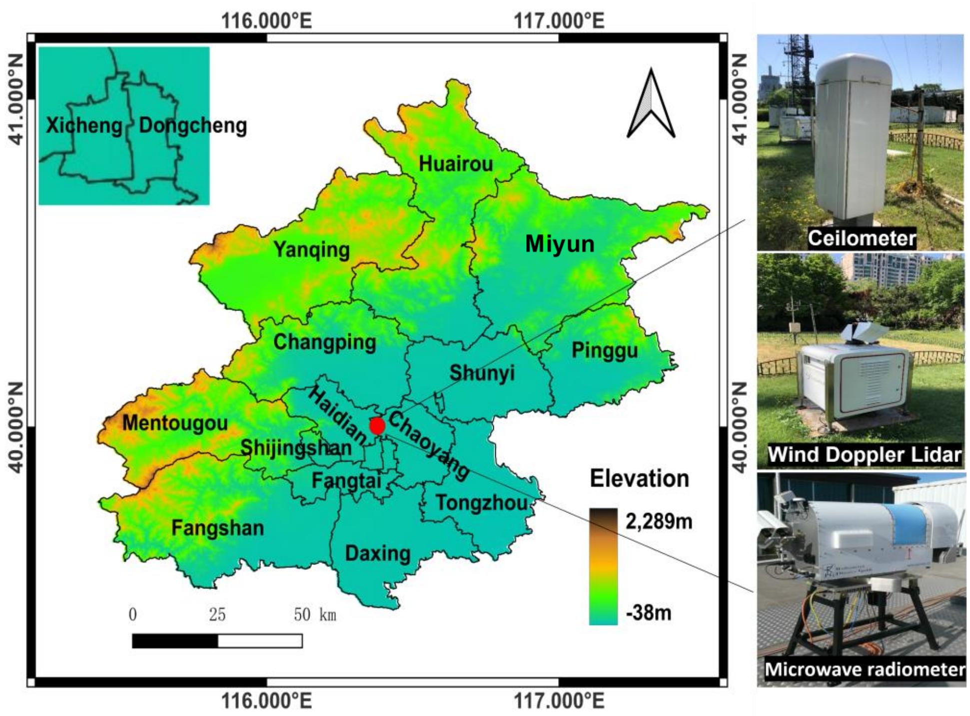

Figure 1. Represent the topographic map of Beijing (left panel). The red dot mark shows observational site and the right panel displays the instruments used for data acquisition.

3 Results and Discussion

To evaluate the seasonal evolution of boundary-layer structure, representative periods from four seasons were selected. Thermal, dynamic, and material PBLHs were analyzed together. using to evaluate their diurnal development, seasonal

https://doi.org/10.5194/egusphere-2026-4121
Preprint. Discussion started: 5 August 2026

differences, day-night contrast, and degree of agreement among three retrieval approaches. Moreover, in order to check the relationship between meteorology and air pollutant with three boundary layer heights.

3.1 Winter: Shallow and stable boundary layers

Figure 2 illustrates the time-height evolution of the three boundary-layer heights during representative winter period of 9-15 December. During the week, the three boundary layers were generally shallow, although they exhibited notable differences in their temporal evolution. The Figure 2a showed that thermal PBLH remained mostly below 1 km, with a weekly mean of 605 m, suggesting limited thermal development during the winter months. Moreover, the structure of $\partial\theta v/\partial z$ indicates frequent stable stratification above the lower layer, consistent with limited wintertime thermal development. Figure 2b shows a broadly analogous temporal development, although dynamic PBLH was consistently higher (particularly at night) with a weekly average of 748 m than thermal PBLH. This implies that wind shear and mechanical turbulence can sustain a deeper dynamically defined layer above the shallow stable surface layer, particularly when high turbulence and stronger winds were present. The material PBLH (Figure 2c) shows a different behaviour, with an average of 635 m, yet it is more influenced by vertical backscatter gradients. The backscattered signal was frequently concentrated within the lower atmosphere (below 1000 m), indicating that aerosols were confined to a shallow layer. Above 1 km, backscatter was generally weak, with intermittent elevated layers discussed separately in the case studies. During daytime, the three PBLHs generally increased from late morning to early afternoon, reaching hourly peak mean values of 1124 m (thermal PBLH),1168 m (dynamic PBLH), and 1285 m (material PBLH). The values show that, even in winter, daytime mixing can deepen the boundary layers up to approximately 1–1.3 km under favourable conditions such as stronger insolation and enhanced mechanical mixing.

In December, two contrasting regimes were noted. During 10 December 18:00–11 December 09:00 BJT, thermal and dynamic PBLH remained significantly elevated, with mean values of 973 m and 1040 m, respectively, while material PBLH averaged only 577 m. This behaviour was favoured by thermal structure (Figure 2a) as the 25-275 m layer remained partially unstable (mean $\partial\theta v/\partial z = -0.263$), overlaying a stable layer (above 800 m), consistent with a deep residual mixed layer above. Consequently, the thermal algorithm identified the upper stable interface of a weakly mixed thermal layer rather than shallow surfaced-based inversion. From dynamic perspective (Figure 2b), the presence of enhanced low-level winds and shear favoured the continuation of mechanical mixing by weakening near-surface stability, which explains why the thermal and dynamic PBLHs were both elevated while material PBLH remained lower. The material PBLH (Figure 2c) indicated vertical decoupling. Backscatter signal above 800 m was strong, but below its intensity decreased. In addition, Cloud-base height (CBH) retrievals revealed frequent elevated cloud bases yet showed no signs of low cloud or fog. Thus, the elevated nighttime thermal and dynamic PBLHs on 10-11 December mainly reflect the residual thermal structure, increased low-level mechanical mixing, and interaction with elevated cloud-aerosol layers.

Conversely, 15 December marked a case of shallow and polluted boundary layer. The daily mean thermal, dynamic, and material PBLHs were 367 m, 333 m, and 587 m. The unstable thermal layer (Figure 2a) was restricted to roughly around 228 m, while the above 300 m layers remained strongly stable, with a mean positive $\partial\theta v/\partial z$. At the same time, low-level mechanical mixing weakened, as indicated by lower daytime wind speed and wind shear observed at 50-300 m (Figure 2b). In Figure 2c,

https://doi.org/10.5194/egusphere-2026-4121
Preprint. Discussion started: 5 August 2026

backscatter signal also increased markedly at 0-800 m. Considering the moderate relative humidity with very low CBH detection on 15 December, the strong signal predominantly indicates the aerosols accumulation under weak surface heating and insufficient dilution conditions.

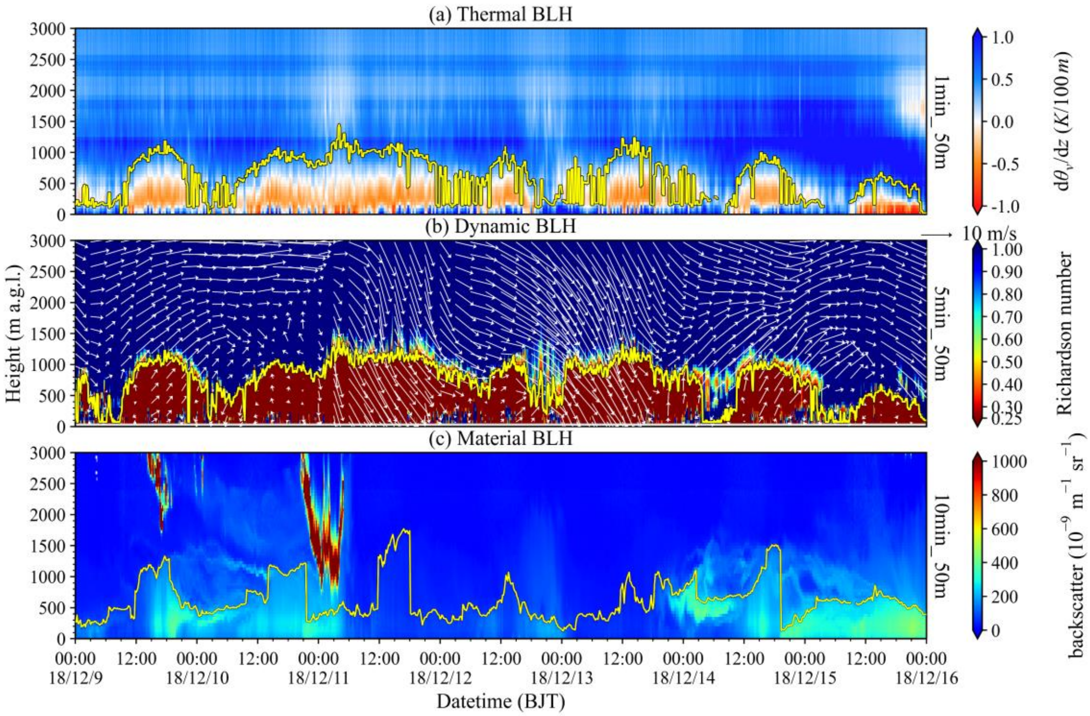

Figure 2. Time–height distributions of (a) ∂θv/∂z and the thermal boundary-layer height, (b) bulk Richardson number (Ri) and the dynamic boundary-layer height. The white arrow is the wind vector and the arrow length represents wind speed at 10 m/s, and (c) ceilometer backscatter coefficient and the material boundary-layer height during a vertical resolution of 50 m with temporal resolution of 1 min/5 min/10 min, respectively. The yellow solid line represents the corresponding PBLH above ground level.

3.2 Spring: Rapid daytime boundary layer growth

Figure 3 shows a pronounced springtime deepening of the boundary layer, with clear daytime growth and nighttime reduction in all three diagnostics. Thermal and dynamic PBLHs exhibited more pronounced development, with weekly mean values of 818 m and 783 m, respectively. In Figure 3a, frequent unstable layer occurred particularly below 300 m. Conversely, the consistent positive gradients observed above 600 m, indicate that vertical development was often limited by stable stratification aloft. The retrieved thermal PBLH grows rapidly after the morning transition and typically reaches 1000–1600 m on well-mixed afternoon periods, with a maximum of 1778 m, before decaying toward a shallow stable layer at night. The dynamic PBLH shows a similar daytime pattern, typically developing to approximately 1000-1300 m during daytime, reaching a maximum of about 1700 m. The Ri structure indicates that turbulence was mostly persistent within the lower 75-300 m. However, during the daytime, the dynamically active layer often extended to about 800-1000 m, signifying a stronger coupling between near-surface mechanical mixing and boundary layer growth. The mean material PBLH had a weekly mean of 896 m, and reached a maximum of 1900 m. The material PBLH during daytime was generally higher (1003 km) than that of night

https://doi.org/10.5194/egusphere-2026-4121
Preprint. Discussion started: 5 August 2026

(760 m). In the material PBLH (Figure 3c), enhanced backscatter was mostly concentrated below 1000 m, indicating elevated aerosol loading within the surface-connected layer.

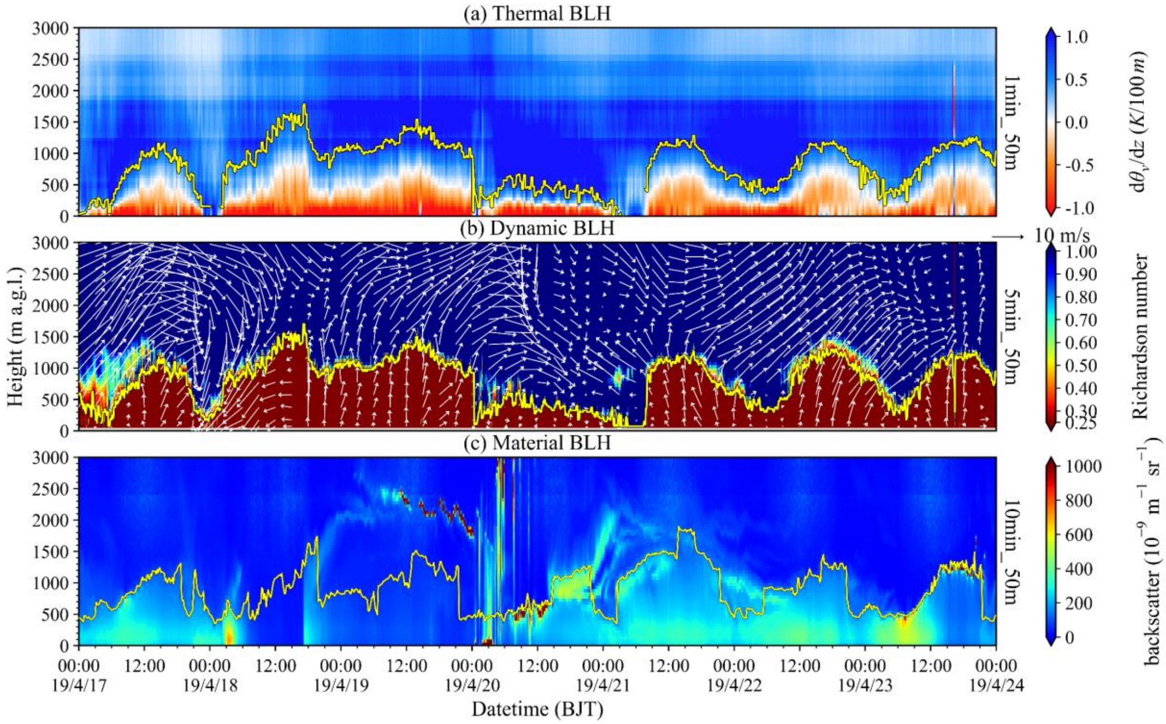

Figure 3. Time–height distributions of (a) ∂θv/∂z and the thermal boundary-layer height, (b) bulk Richardson number (Ri) and the dynamic boundary-layer height, while the white arrow is the wind vector and the arrow length represents wind speed at 10 m/s, and (c) ceilometer backscatter coefficient and the material boundary-layer height during a vertical resolution of 50 m with temporal resolution of 1 min/5 min/10 min, respectively. The yellow solid line represents the corresponding PBLH above ground level.

In contrast, 20 April exhibited a significant daytime collapse. The thermal PBLH dropped to 460 m. Relative to 19 April, the 0-300 m layer was 4.37 K colder, while the 300-800 m and 800-1200 m were 4.47 K and 5.88 K warmer respectively. The warm over cold structure created a strong stable cap and the ∂θv/∂z field showed that the negative gradient layer was confined to approximately 186 m, while above 300 m remained strongly stable. The Dynamic PBLH also decreased to 421 m, as the low-level mechanical mixing had considerably weakened. Relative to the daytime of 19 April, the wind speed dropped by 50 to 60% below 800 m layer, while the shear in the 50-300 m layer has also reduced by 50%. Thus, the dynamic collapse was not only by thermal stability but also by a reduction in wind-driven mixing in the lower atmosphere. Although the thermal and dynamic PBLH collapsed below 500 m, material PBLH remained higher at 815 m. The discrepancy noted coincided with a rise in humidity level, where relative humidity increases from 37% to 81% below 800 m. Additionally, the absolute humidity increased by 49%. This indicates the presence of enhanced humidified aerosol or particles affected by clouds in a shallow,

https://doi.org/10.5194/egusphere-2026-4121
Preprint. Discussion started: 5 August 2026

surface connected layer. Overall, the low PBLH episodes observed on 20 April can be attributed to significant thermal capping, reduced mechanical mixing in the lower atmosphere, and increase in aerosol and cloud-affected particles in the lower layer under humid conditions.

3.3 Summer: Strong thermal, dynamic, and material PBLH coupling

The July case (Fig. 4) exhibits the deepest and most persistent daytime boundary-layer development among the seasons, characterized by a classic convective growth–collapse cycle. In Figure 4a, thermal PBLH rises rapidly after the morning transition and frequently sustains a deep mixed layer through the afternoon and early evening, averaging about 1004 m and reaching a maximum of about 1995 m. consistent with strong surface buoyancy forcing in midsummer. During the daytime, the unstable layer (negative $\partial\theta v/\partial z$) extended from 25-300 m and persisted through 300-800 m. In contrast, nighttime instability was confined to below 300 m. The high daytime unstable layer enabled the thermal PBLH to grow substantially deeper. In Figure 4b, dynamic PBLH typically shows a similar daily pattern. During the period of intense convection, mechanically driven turbulent layer reached a depth of about 995m, comparable to the thermodynamic mixed layer. The daytime turbulence conditions commonly extending to about 1500 m and occasionally deeper, whereas nighttime turbulence became considerably shallower, remaining below 400 m after midnight. Wind speeds remained moderate in the 50-300 layer (2.76 m s^{-1}) and above 300 m (3.75 m s^{-1}), with moderate to weak shear, indicating that the July dynamic PBLH was mainly sustained by convective conditions, while mechanical mixing offering additional, secondary support. Unlike the thermal and dynamic PBLHs, the material PBLH (Figure 4c) is generally shallower during peak mixing, indicating that the "well-mixed tracer layer" defined by aerosols typically ends beneath the top of the thermodynamic/dynamic boundary layer, particularly when aerosols become diluted due to strong vertical mixing and upward transport and the vertical gradients in backscatter become weak. The average material PBLH around 841 m with a maximum reaching 2600 m. The backscatter field indicates that the persistent signal was mainly concentrated below 800 m, especially within the lowest 300 m, however it was not consistent over the week. Increased backscatter layers were also observed, particularly in the 800-1500 m on July 7 and above 1500 m on July 9.

The July 9 case was a special cloud-affected decoupling event. The thermal retrieval indicated a suppression of buoyant growth, with thermal daytime PBLH at 778 m, and the unstable layer limited to below 200m. the dynamic retrieval indicated weak mechanical mixing, with daytime dynamic PBLH at 630 m under reduce wind speed and shear (Figure 4b). The interaction of this process is evident: the cloud-induced reduction in heating weakened convection, whereas the weak shear restricted both entrainment and vertical mixing. This is consistent with previous Sichuan Basin study showing that cloud-radiation interaction (CRI) can reduce daytime PBLH by about 50% under cloudy conditions (Lu et al., 2024). The daytime material PBLH retrieved from backscatter was even lower at about 400 m. During this time, the frequent detection of CBH, points to the persistent influence from clouds. Therefore, the strong backscatter extending upward was likely influenced by cloud droplets, or cloud contaminated layers instead of representing a well-mixed aerosol BL. Thus, July 9 was a cloud-affected multilayer case rather than a simple shallow pollution event.

https://doi.org/10.5194/egusphere-2026-4121
Preprint. Discussion started: 5 August 2026

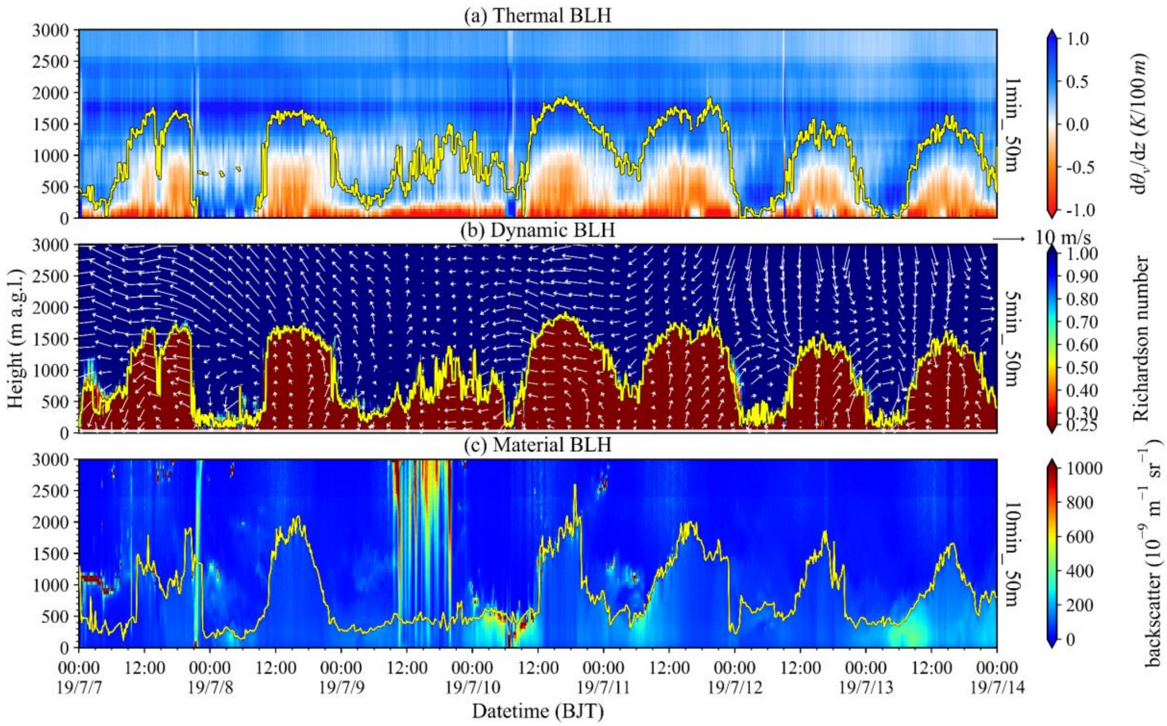

Figure 4. Time–height distributions of (a) ∂θv/∂z and the thermal boundary-layer height, (b) bulk Richardson number (Ri) and the dynamic boundary-layer height, while the white arrow is the wind vector and the arrow length represents wind speed at 10 m/s, and (c) ceilometer backscatter coefficient and the material boundary-layer height during a vertical resolution of 50 m with temporal resolution of 1 min/5 min/10 min, respectively. The yellow solid line represents the corresponding PBLH above ground level.

3.4 Autumn: Transitional regime and early evening collapse

Fig. 5 shows evolution of thermal, dynamic, and material PBLHs but with a more pronounced transitional character, featuring continued daytime development, with more distinct nighttime stabilization and earlier post-sunset collapse than in summer. During the week, thermal PBLH recorded an average of 770 m, with a peak reaching around 1995 m. The thermal PBLH (Figure 5a) exhibits repeated daytime growth followed by nighttime suppression. The ∂θv/∂z indicates a strongly unstable layer persistently below 300 m, whereas during the daytime this unstable layer often extends upward to 800 m, facilitating further deepening above 1000 m. The dynamic PBLH (Figure 5b) was closely aligned with the thermal PBLH. The mean dynamic PBLH 750 m, peaked at 2003 m, and after midnight it decreased to 299 m, indicating that nocturnal stability suppressed vertical coupling despite stronger winds aloft (3.54-6.23 m s^{-1} from 50-1500 m). Generally, material PBLH (Figure 5c) followed the daily growth-decay pattern, but tends to be lower than thermal and dynamic PBLHs throughout the day, with a mean value of 669 m, reflecting its dependence on the vertical distribution of aerosol backscatter. The backscattered was mainly concentrated below 800 m, indicating that aerosol layer linked to the surface was often shallow. However, elevated

https://doi.org/10.5194/egusphere-2026-4121
Preprint. Discussion started: 5 August 2026

backscattered structures were observed intermittently above 800 m, notably on 14 September, consistent with an elevated aerosol-layer signature and during the deeper material-layer conditions observed on 16-17 September. Conversely, September 15th demonstrated a sustained low material PBLH, reflect weak vertical mixing of aerosol and a very shallow surface-connected material layer.

Two September subperiods require separate diagnosis. The anomaly observed on 13 September (00:00-6:00 BJT) was strongly influenced by Rain Flag conditions, suggesting contamination in the retrieval. The presence of rain and clouds during this timeframe further elucidates the very low material PBLH during that day. During 17 September 23:00–18 September 03:00 BJT, an unstable layer persisted below 200 m (Figure 5a), likely representing residual daytime heat from mixing, which allowed the parcel-method thermal PBLH to respond to the upper thermal transition rather than collapse to a very shallow surface layer. The elevated nocturnal dynamic PBLH (Figure 5b) supported by strong wind-driven turbulence. Wind speed rose from around 3.45-10.97 m s^{-1} in the 50-1500 m. Consistently, Ri <0.25 occurred throughout below 1000m layer, indicated the strong shear-related turbulence allowed dynamic PBLH to rise to around 1000 m at night.

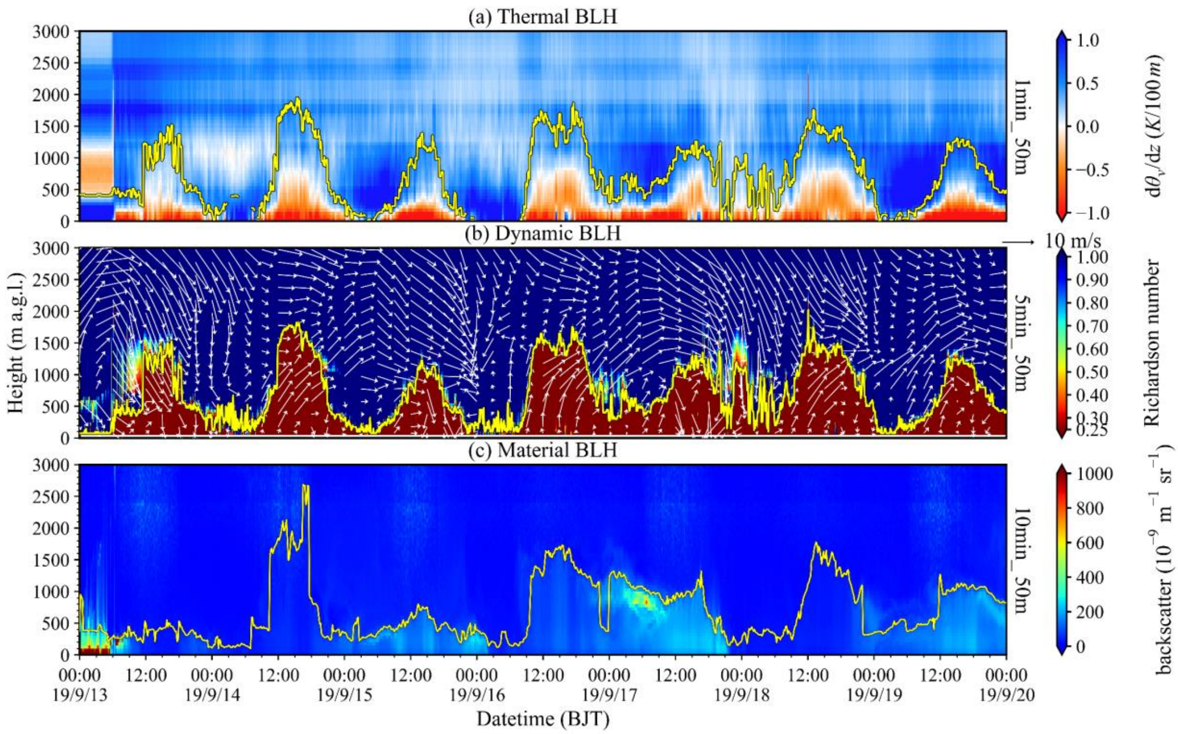

Figure 5. Time–height distributions of (a) ∂θv/∂z and the thermal boundary-layer height, (b) bulk Richardson number (Ri) and the dynamic boundary-layer height, while the white arrow is the wind vector and the arrow length represents wind speed at 10 m/s, and (c) ceilometer backscatter coefficient and the material boundary-layer height during a vertical resolution of 50 m with temporal resolution of 1 min/5 min/10 min, respectively. The yellow solid line represents the corresponding PBLH above ground level.

3.5 Seasonal and diurnal characteristics of PBLHs and air pollutants

3.5.1 Seasonal, day-night, and diurnal variability of PBLHs

https://doi.org/10.5194/egusphere-2026-4121
Preprint. Discussion started: 5 August 2026

The three PBLHs showed distinct seasonality. In December, dynamic PBLH recorded the highest seasonal mean (828 ± 386.9 m), followed by thermal PBLH (666 ± 357.4 m) and material PBLH (625 ± 387.1 m). Diurnal median maxima (Figure 6a) occur in the afternoon. The thermal PBLH peaked at 951 m at 14:00, the dynamic PBLH reached 1068 m at 16:00, and the material PBLH peaked at 1006 m at 15:00, indicating increased daytime turbulence and the development of aerosol layers. During April, seasonal mean values of dynamic and material PBLHs were higher (871 ± 408.9 m and 918 ± 472.2 m) than thermal PBLH (657 ± 411.4 m). The peak diurnal medians (Figure 6b) were recorded at 1019 m at 13:00 for thermal PBLH, 1142 m at 15:00 for dynamic PBLH, and 1331 m at 18:00 for material PBLH, indicating a more pronounced development of PBLH in spring and a delayed growth of the material PBLH. In July, thermal PBLH was highest with a mean value of 804 ± 408.9 m followed by material PBLH (795 ± 512.9 m) and dynamic PBLH (722 ± 538.5). The diurnal cycle was strongest in July (Figure 6c) with peaked median values of 1397 m for thermal PBLH at 13:00, 1402 m and 1464 m for dynamic and material PBLHs at 16:00 BJT, reflecting strong summertime daytime development.

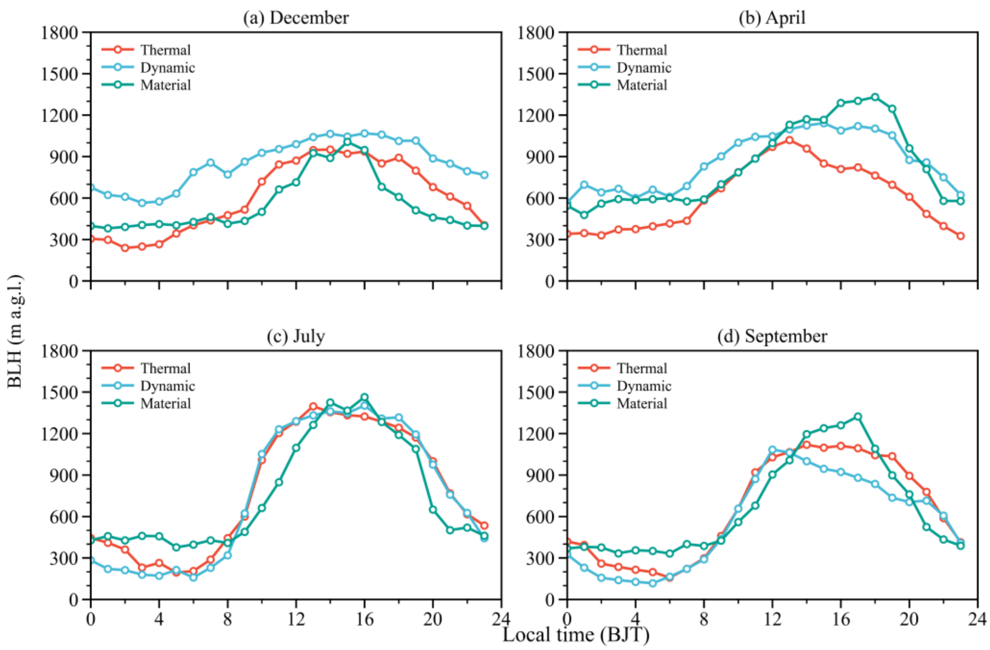

Figure 6. Monthly diurnal variation of thermal, dynamic , and material boundary layer height for (a) December, (b) April, (c) July, and (d) September.

Compared to July, September showed a decline in seasonal mean values with thermal, dynamic and material PBLHs averaging 685 ± 415.7 m, 591 ±414.5 m, and 709 ± 442.4 m respectively. Although the PBLHs generally declined from July to September, both months still showed high thermal and material PBLH values than the dynamic PBLH. This indicates that enhanced surface heating supported buoyancy-driven growth and convective transport, enabling the thermally developed and pollutants containing layers to rise above the dynamic PBL top. The highest diurnal variation (Figure 6d) was observed at 14:00 for thermal PBLH at 1119 m, at 12:00 for dynamic PBLH at1083 m, and at 17:00 for material PBLH at 1323 m. This

https://doi.org/10.5194/egusphere-2026-4121
Preprint. Discussion started: 5 August 2026

indicates a transition-season regime with substantial but weaker daytime growth and a subsequent of the material PBLH later in the day. The day-night contrast (Figure 7) was consistent with diurnal median pattern. In December, median nighttime values were 485 m (thermal PBLH), 800 m (dynamic PBLH), and 418 m (material PBLH), increasing to 838, 992, and 633 meters during the day. During April, the increases recorded were from 386 m to 730 m for thermal PBLH, from 750 m to 1001 m for dynamic PBLH and from 655m to 970 m for material PBLH, reflecting stronger development during the daytime in Spring. July exhibited the most pronounced contrast for thermal and dynamic PBLHs, with thermal PBLH increasing from 461 to 1047 m and dynamic PBLH from 289 to 1001 m, while material PBLH increase from 463 to 845 m. In September, the enhancement of daytime conditions was notable, as thermal, dynamic, and material PBLHs increasing from 443 m, 388 m, and 390 m at night to 885 m, 713 m, and 884 m during the daytime respectively, reflecting a transition-season regime with substantial but weaker daytime growth than midsummer.

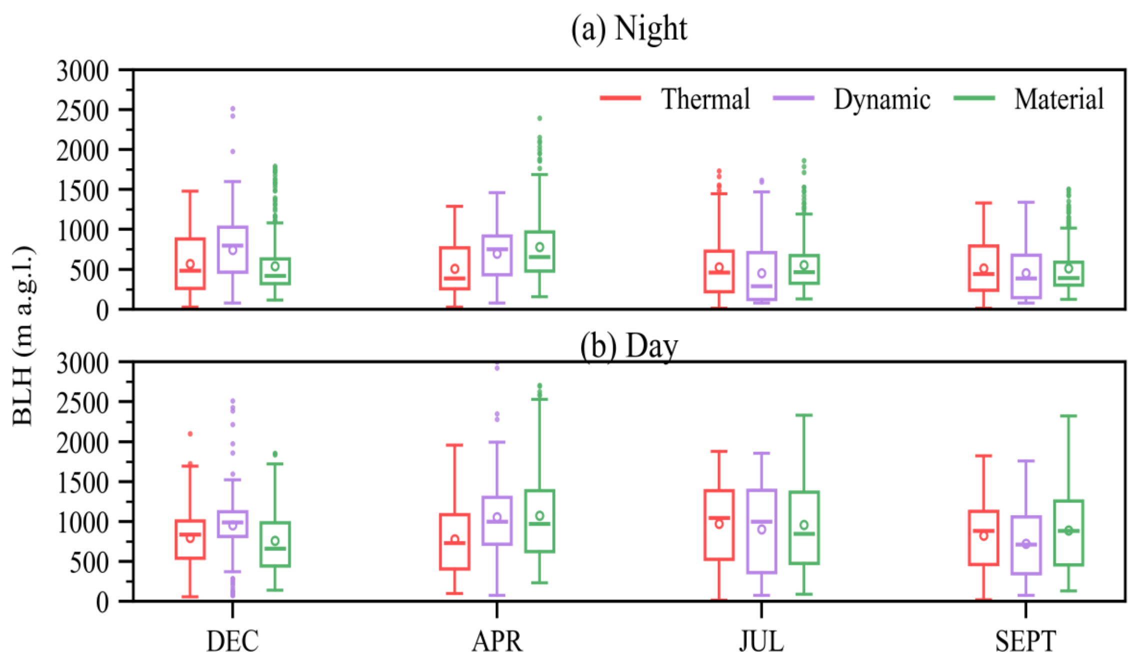

Figure 7. Seasonal day and night contrast among thermal, dynamic, and material boundary layer heights. Box plot with the first and third quartile representing the upper and lower bound. The central line represents the median values and circle represent the mean values. The vertical whiskers extended from the box represent the spread of data equal to 1.5 times the interquartile range. The dots represent the outliers.

3.5.2 Seasonal, day-night, and diurnal variability of air pollutants

The four distinct periods exhibited evident seasonal variations between primary pollutants and photochemical oxidants. In April, $PM_{2.5}$ and PM_{10} reached their maximum levels, with an average concentration of 49.0 ± 34.5 and 94.0 ± 68.1 μg m^{-3}, respectively. December also showed relatively high particulate concentrations, with an average $PM_{2.5}$ and PM_{10} reaching 45.1± 46.6 and 86.9 ± 64.7 μg m^{-3}. Monthly mean Concentrations of NO_2 (52.5 ± 29.5 μg m^{-3}), SO_2 (7.2 ± 4.3 μg m^{-3}), and CO (0.917 ± 0.629 mg m^{-3}) peaked in December, indicating enhanced primary-pollutant accumulation under weak wintertime dispersion.

https://doi.org/10.5194/egusphere-2026-4121
Preprint. Discussion started: 5 August 2026

O_3 exhibited contrasting seasonal trend, peaking in July and September with monthly mean values of 102.9 ± 62.37 and 89.59 ± 64.24 µg m^{-3}, reflecting enhanced warm-season photochemical production. The day-night differences (Figure 9) further highlighted the seasonal contrast. Ozone was consistently higher during the day time in every month, whereas, NO_2 generally increased during the nighttime. Conversely, $PM_{2.5}$ and PM_{10} were seasonal dependent, with $PM_{2.5}$ being higher during daytime in April, July, and September, but higher at night in December. In contrast, PM_{10} showed higher levels during the day only in April, while its was more pronounced at night in December, July, and September. SO_2 and CO showed relatively small day-night differences, with only modest seasonal variation. The diurnal peak timing illustrated in Figure 7 further reinforces the seasonal differences across hourly evaluations. O_3 consistently reached its peak levels in the afternoon (15:00-16:00 BJT), with peak mean values of 42 µg m^{-3} (December), 111 µg m^{-3} (April), 167 µg m^{-3} (July), and 162 µg m^{-3} (September). In contrast, PM_{10}, $PM_{2.5}$, NO_2, and CO generally peaked in the late night to early morning transition (Figure 8). SO_2 peak during daytime in April, July, and September, indicating potential influences from regional transport or the downward dispersion of increased industrial emissions (Wang et al., 2023; Xin et al., 2024). The comparative low SO_2 concentrations during the warm season are consistent with the long-term decline in coal combustion and the effect of regional emission controls policies in Beijing (Vu et al., 2019). Overall, the diurnal analysis underscores the seasonal shift from the accumulation of primary pollutants in winter nights to episodic occurrences in spring and finally to the dominance of photochemical O_3 in summer and early autumn.

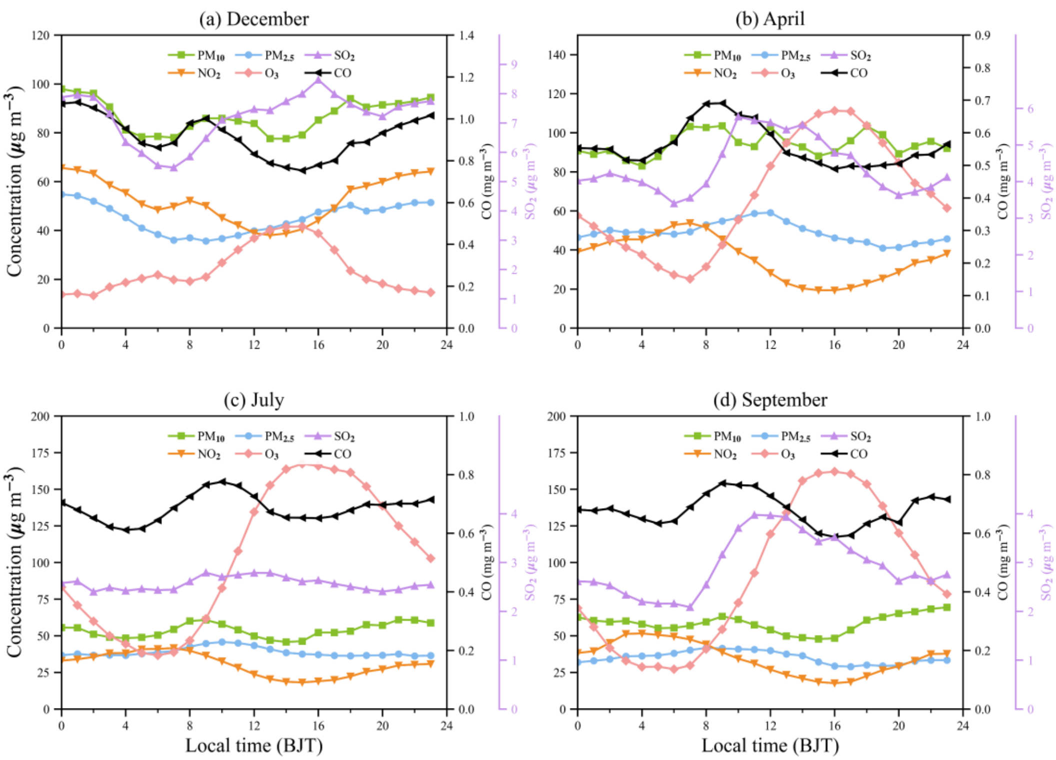

Figure 8. Monthly diurnal variation of air pollutants for (a) December, (b) April, (c) July, and (d) September.

https://doi.org/10.5194/egusphere-2026-4121
Preprint. Discussion started: 5 August 2026

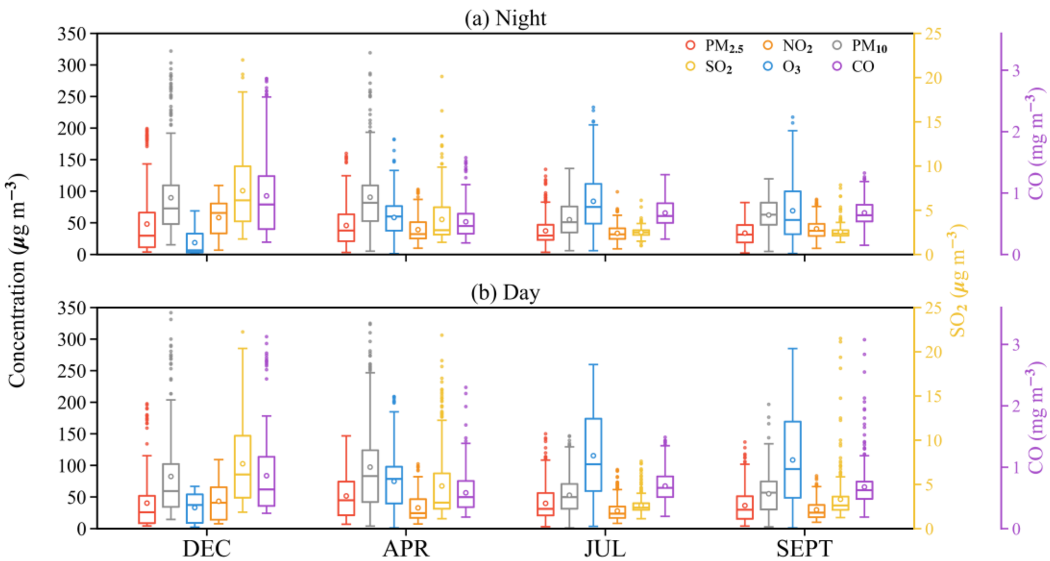

Figure 9. Seasonal day and night contrast of air pollutants. Box plot with the first and third quartile representing the upper and lower bound. The central line represents the median values and circle represent the mean values. The vertical whiskers extended from the box represent the spread of data equal to 1.5 times the interquartile range. The dots represent the outliers.

3.6.1 Seasonal variation in PBLH-Pollutant relationships

The seasonal correlations show a consistent dilution pattern for primary pollutant during the colder and transitional months, but this relationship weakened in the warm season (Table S1). During December, PM_{10}, $PM_{2.5}$, NO_2, SO_2, and CO were significantly and negatively (ρ = -0.47 to -0.74) correlated with dynamic PBLH. Thermal PBLH also showed significant correlations, yet the magnitudes (ρ = -0.33 to -0.6) were generally weaker than dynamic PBLH. This implies that a significant role of the PBL in controlling pollutant accumulation in winter month. A similar, albeit weaker trend was evident in April, where dynamic PBLH remained a primary influence on $PM_{2.5}$ (ρ = -0.33), NO_2 (ρ = -0.68), and CO (ρ = -0.45). Conversely, July and September exhibited weaker relationship between all three PBLHs and PM_{10} and $PM_{2.5}$, however, NO_2 continue to show a robust and negative correlation with material and thermal PBLHs in both July (ρ = -0.55 and -0.56) and September (ρ = -0.58 and -0.59). Ozone exhibited a positive correlation with all three PBLHs across every month, with notably weaker associations observed in April. Thermal and dynamic PBLHs were most pronounced in December (ρ = 0.66 and 0.77), while with material PBLH, much stronger relationship in July and September (ρ = 0.6). The seasonal variation in PBLH-pollutant relationship suggest that boundary-layer structure plays a key role in regulating near-surface air quality across different seasons. These results suggests that weak surface heating and diminished thermal buoyancy in winter, limited convective growth and vertical mixing. As a result, the upward transport of pollutants into the free atmosphere is restricted, whereas dynamically driven processes maintained a comparatively deeper boundary layer. Consequently, pollutants tend to remained trapped within lower atmosphere, promoting local accumulation and pollution buildup. In contrast, deeper boundary layer growth in warm season enhances turbulent ventilation and promote more efficient upward transport of pollutants, thereby weakening the near-surface PM-PBLH relationship. The positive correlations between ozone and PBLH in this study likely reflect the combined

https://doi.org/10.5194/egusphere-2026-4121
Preprint. Discussion started: 5 August 2026

effects of stronger convective mixing and enhanced in situ ozone formation under deeper boundary-layer conditions. Overall, the observed seasonal trend reveals a dominance of dynamic PBLH-driven dilution in the winter and spring, contrasted with a more substantial thermal-material PBLHs impact on NO_2 and O_3 in summer and early autumn seasons.

3.6.2. Regime-Dependent Boundary Layer Height-Pollutant interactions

To assess whether pollutants were correlated with boundary layer height compression or recovery, representative multihour periods were identified based on the simultaneous behaviour of the three PBLHs and the near surface pollutants. For each selected interval, the relative change factors from start to end were separately calculated for thermal, dynamic, and material PBLHs and for the air pollutants.

In December (Figure 10), A2 exhibited the most pronounced accumulation regime, as thermal, dynamic, and material PBLHs sharply decreased, while $PM_{2.5}$, SO_2, NO_2, and CO increased concurrently, and O_3 concentrations declined. This pattern indicates strong vertical confinement and a build-up of primary pollutants. A1 also showed an upward trend in PM, SO_2, NO_2, and CO, without a substantial decrease in PBLH, particularly in the dynamic PBLH, indicating that the accumulation was mainly due to reduced thermal and vertical mixing. Conversely, A3 should be interpreted as a polluted maintenance phase within a shallow PBLH, because pollutant concentrations were already elevated and the relative changes from beginning to end were less pronounced. D1 and D2 represent the pollutant removal phase, during which primary pollutants concentrations decreased while O_3 increased, aligning with improved dilution and recovery of daytime photochemical conditions. During these phases, thermal and dynamic PBLHs increased, whereas material PBLH showed the weak tendency. Overall, the winter pattern is consistent with prior studies showing that weak turbulence, low PBLH, stable stratification, and inadequate ventilation facilitate the accumulation of heavy $PM_{2.5}$ pollution (Tang et al., 2016; Zhang et al., 2020; Zhang et al., 2021).

The relationship between PBLHs and pollutants became increasingly complex in April. Evening events continued to show accumulation patterns, particularly A1 and A2, during which the collapse of all three PBLHs coincided with increases in NO_2, CO, and PM, together with the reduction of O_3. However, April also included pollutant events that were not directly associated with PBLHs collapse. In S1, thermal and dynamic PBLHs decreased, while pollutant concentrations increased, whereas material PBLH showed the opposite trend. By contrast, in S2 all three PBLHs increased as did most pollutants except NO_2, which decreased. The concurrent increase in SO_2 and O_3 in S2, in the absence of PBLH collapse, indicated regional or elevated-source influence. Its PM_{10}-rich composition further indicated an additional contribution from coarse particles or resuspension. D1 represented a clear dilution and recovery phase, with thermal, dynamic, and material PBLHs increasing by a factor of 2.6-3.0, while $PM_{2.5}$, PM_{10} NO_2, SO_2, and CO concentrations decreased and O_3 increased by a factor of 7 (Figure 11), reflecting enhanced vertical mixing and daytime photochemical activity.

In July, D1 demonstrated the most pronounced daytime recovery pattern. Thermal, dynamic, and material PBLHs increased markedly, while $PM_{2.5}$ and NO_2 decreased and O_3 increased by a factor of 7.6 (Figure 12). In A1, all three PBLHs decreased especially the material PBLH, coinciding with increases in PM_{10}, NO_2, and CO and a reduction in O_3. A2 displayed a similar trend, with thermal, dynamic, and material PBLHs decreasing by factors of 5.0, 3.7, and 7.1, respectively. A3 represented an additional accumulation subtype, in which PBLHs collapse was associated with increased pollutant concentrations except SO_2,

https://doi.org/10.5194/egusphere-2026-4121
Preprint. Discussion started: 5 August 2026

which decreased, suggesting partial decoupling from the primary accumulation signal. These events imply that the accumulation of nocturnal primary pollutants was favoured when thermal, dynamic, and material PBLHs became shallower, although the increase in $PM_{2.5}$ was less significant than that in December. In contrast, S2 illustrated distinct mixing/transport-photochemical regime, characterized by strong PBLHs growth, substantial O_3 enhancement, elevated SO_2, and decreased NO_2.

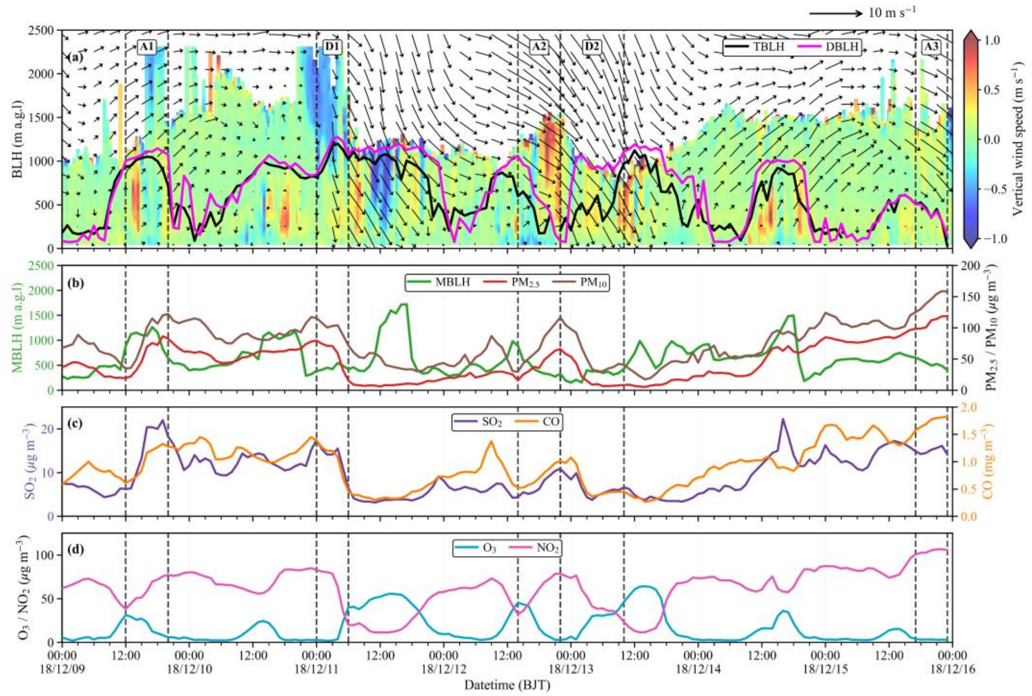

Figure 10. Comparison of amplitude changes between initial and late stages of boundary layer heights-pollutant interaction periods in (a) thermal and dynamic PBLH, black arrow is the wind vector and the arrow length represents wind speed at 10 m/s and the background color is the vertical wind speed (b) material PBLH, PM2.5, and PM10, (c) SO2, and CO (d) NO2, and O3 during December week in Beijing.

In September (Figure 13), the PBLH-pollutant coupling showed the clearest alternating pattern. In A1, thermal, dynamic, and material PBLHs saw a sharp decrease, whereas primary pollutants increased and O_3 decreased, indicating evening accumulation under shallow mixing conditions. A2 showed an even stronger collapse, representing the clearest case of PBLHs compression and pollutant accumulation observed in September. D1 represented a conventional daytime recovery phase with all three PBLHs increased, while $PM_{2.5}$, NO_2, and CO decreased, reflecting enhanced dilution. S1 also exhibited a photochemical regime, characterized by a rapid O_3 enhancement as PBLHs increased and NO_2 declined. However, the absence of simultaneous decreases in PM levels suggests that aerosol variability was not solely controlled by dilution. S2 and S3 exemplified non-collapse scenarios. In S2, both PM fractions increased, despite PBLHs growth and substantial O_3 enhancement, suggesting additional influences such as transport, secondary formation, or coarse-particle processes. In S3, simultaneous increases in SO_2, PM, and O_3, coupled with a decline in NO_2 under deepening PBLHs, imply that SO_2/PM enhancement was probably not caused by local PBLHs compression, but more plausibly due to daytime mixing or regional transport.

https://doi.org/10.5194/egusphere-2026-4121
Preprint. Discussion started: 5 August 2026

Previous studies have shown that the air quality in Beijing is strongly influenced by regional transport, with pollution episodes often associated with southerly airflows from high-emission zones in the North China Plain, particularly via southwest and southeast transport pathways. In contrast, clean air conditions are generally associated with northerly ventilation (Zhang et al., 2012; Wang et al., 2021; Yin et al., 2025). To evaluate this mechanism, we examined the wind direction during the selected accumulation, dispersion, and mixed cases for each month. December and July showed the clearest consistency with this framework. Accumulation events (Figure S1) were largely governed by S-SW flow, whereas dilution (Figure S2) events were predominantly associated with N-NW or northerly flow. In September, accumulation cases were primarily linked to the SW-W sectors, while D1 (dilution) was dominated by NE-N flow. April showed less directional separation. The dominant pathways for accumulation events were S and NE, while dilution occurred in S-SW flow, a pathway generally linked with polluted transport in Beijing. In these cases, the increase in PBLHs was sufficient to reduce most primary pollutants (except SO_2), suggesting that local vertical mixing overwhelmed the transport effect. For the mixed S cases (Figure S3), April was characterized by easterly and south-easterly winds during S1 and S2. July showed a combination of southerly, south-westerly, and easterly winds in S1 and S2. Finally, September was influenced by south-westerly and north-easterly winds in S1, S2, and S3. Overall, these results point to the conclusion that polluted and mixed conditions were linked to specific seasonal wind patterns. This is consistent with previous studies in Beijing that indicated that wind direction plays a crucial role in the movement and build-up of pollution (Yang et al., 2016).

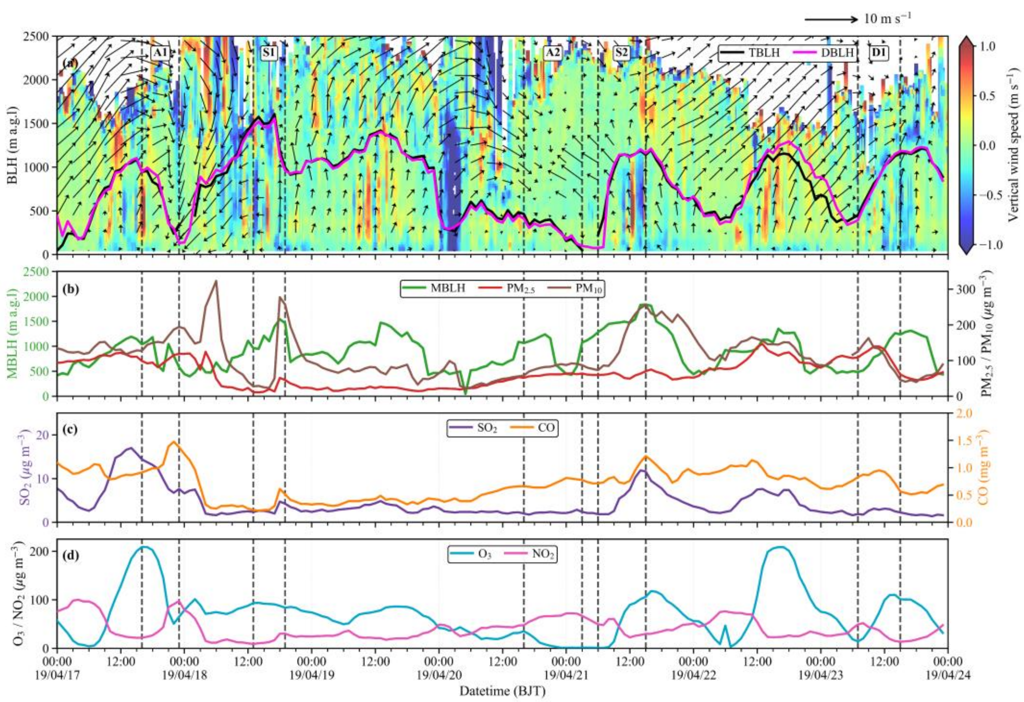

Figure 11. Same as figure 10 but in April week

https://doi.org/10.5194/egusphere-2026-4121
Preprint. Discussion started: 5 August 2026

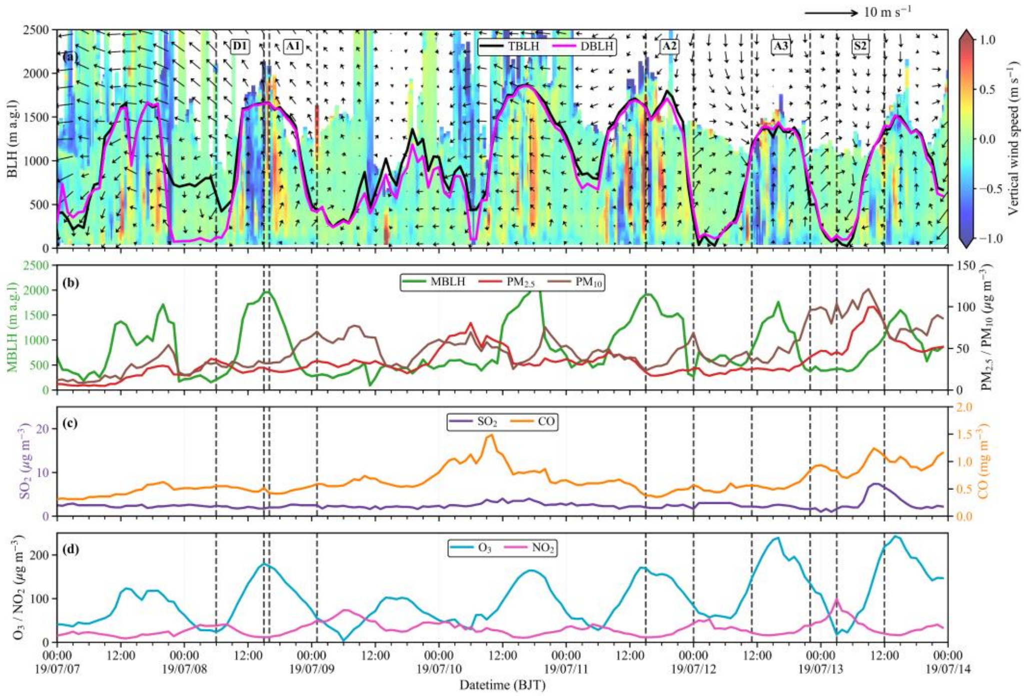

Figure 12. Same as figure 10 but in July week.

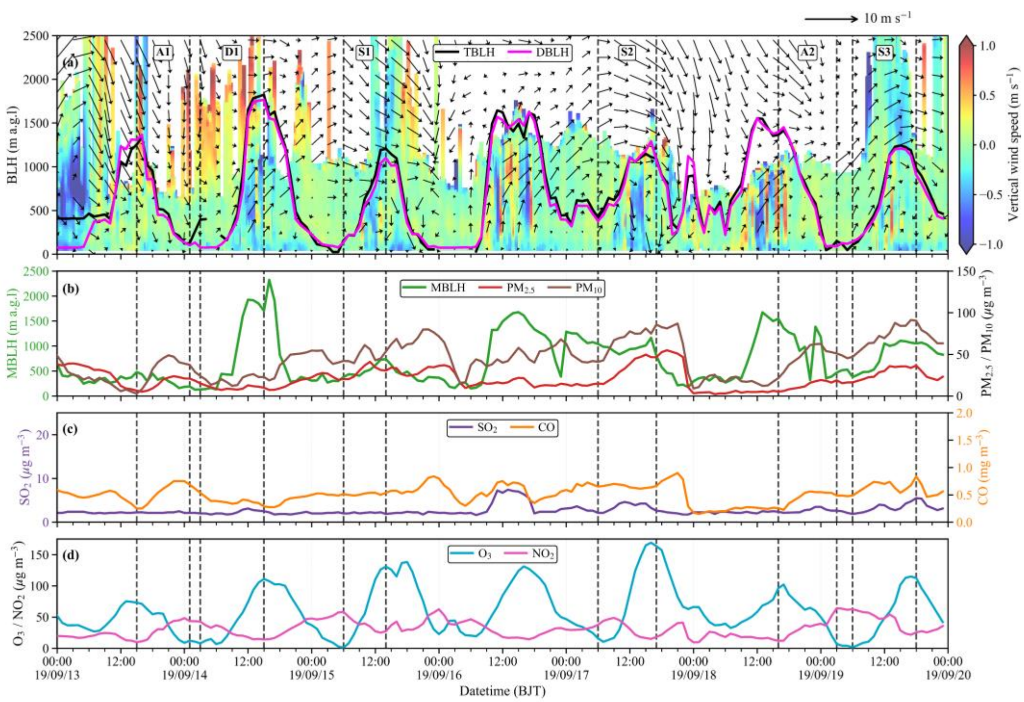

Figure 13. Same as figure 10 but in September week.

https://doi.org/10.5194/egusphere-2026-4121
Preprint. Discussion started: 5 August 2026

4. Conclusions

This study provides a multi-instrument evaluation of thermal, dynamic, and material boundary layer heights (PBLHs) over Beijing, highlighting their physical differences despite their interrelated nature. These differences provide valuable insights into the processes that govern exchange among the surface layer, residual layer, and free troposphere. The comparison across winter, spring, summer, and autumn periods shows that these three PBLHs either converge or diverge depending on season, time of the day, meteorology, aerosol structure, and pollutant regime.

Winter was characterized by moderate PBLHs although mechanically generated turbulence often maintained a deeper dynamic layer than the thermally defined layer especially at night. In spring, rapid daytime BL development and high aerosol-layer variability led to frequent offsets between material and thermal/dynamic estimates. Whereas, in spring, summer, and autumn, the dynamic and thermal PBLHs remained tightly coupled during convective conditions. This implies that when strong convective conditions are present, both parcel and Richardson number methods determine a comparable mixed-layer depth. However, the material PBLH was lower in summer and autumn, indicating the aerosol gradient layer did not always reach the full height of thermal and dynamic PBLHs. The day-night analysis further emphasizes the importance of separating daytime and nighttime BL regimes. Daytime PBLHs were consistently higher across seasons due to stronger surface heating, turbulence, and vertical mixing, whereas nighttime PBLH were more variable. In winter and autumn, residual thermal structure and mechanically turbulence sometimes limited the collapse of thermal and dynamic layers. By contrast, material PBLH was sensitive to aerosol confinement, humidity, cloud effect, causing it differs from thermal and dynamic PBLHs depending on particle distribution and meteorological conditions.

The relationship between PBLH and air pollutant also varied strongly by season and pollutant types. Particulate matter, NO_2, and CO were significantly and negatively correlated with dynamic PBLH in December and April. In July and September, $PM_{2.5}$, PM_{10} showed weak or insignificant correlations with all PBLHs, while SO_2 was weakly related in July but became moderately and positively correlated with all PBLHs in September ($\rho = 0.368–0.406$), likely from residual or transported elevated layers to the surface. Case-based analysis demonstrates that pollution episodes were controlled by both local BL compression and horizontal transport. Accumulation periods were typically associate with decreasing thermal, dynamic and material PBLHs, increasing primary pollutant and decreasing ozone, whereas deeper PBLHs in the daytime facilitate dilution and increased ozone production. However, several mixed cases showed increasing PM, SO_2, or O_3 despite PBLH growth, indicating the influence of regional transport, elevated sources, secondary formation, and photochemistry. Wind direction analysis further supports the interpretation. Polluted and mixed conditions were often linked to southerly, south-westerly, or seasonally dependent transport pathways, whereas cleaner dilution periods were more commonly associated with northerly ventilation.

This study presents a comprehensive multi-instrument comparison of thermal, dynamic, and material boundary layer heights (BLHs) over Beijing, revealing pronounced differences arising from their distinct physical definitions and retrieval mechanisms. The three BLHs exhibit strong seasonal and diurnal variability, with shallow, mechanically driven boundary layers dominating in winter, deep convective and strongly coupled structures in summer, and transitional behaviours in spring and autumn characterized by frequent decoupling. The material BLH is generally lower and more sensitive to aerosol, humidity, and cloud effects, while the dynamic BLH reflects mechanically induced turbulence and may exceed the thermal BLH under stable conditions; the thermal BLH primarily represents buoyancy-driven mixing. The relationship between BLH and air quality is highly season-dependent, with strong negative correlations between BLH and primary pollutants in cold seasons and weaker or negligible relationships in warm seasons, while ozone consistently increases with boundary layer development. Pollution episodes are jointly controlled by boundary layer compression, turbulence intensity, and regional transport pathways. Overall, the multi-BLH framework provides a more physically complete description of urban atmospheric mixing than any single BLH metric, offering improved insight into boundary-layer–pollution interactions and supporting more accurate air quality assessment in complex megacities like Beijing.

Code and data availability

Surface $PM_{2.5}$, PM_{10}, and trace gas observation data used in this study were obtained from the China National Environmental Monitoring Centre, available at https://www.cnemc.cn/en/ last access April 15 2026. Other datasets are available from the corresponding author upon reasonable request.

Supplement link

The link to the supplement will be included by Copernicus, if applicable.

Author contributions

JX and MA conceptualized the study. JX, YM, and YT curated the data. JX and MA conducted the formal analysis. JX, MA, and GT developed the methodology. MA and YT implemented the software. JX and YM provided supervision. YM and DZ performed validation. JX, and MA wrote the original draft. LY, YQ, XR, MA,YM, JC, JX, and GT contributed to writing, review, and editing.

Competing interests

The authors declare that they have no conflict of interest.

Acknowledgements

This study was supported by National Key R&D Program of China (2022YFF0802501), the CAS Strategic Priority Research Program (XDB0760102), the National Natural Science Foundation of China (42475180; 42305090).

Review statement

The review statement will be added by Copernicus Publications listing the handling editor as well as all contributing referees according to their status anonymous or identified.

References

Barlow, J. F., Dunbar, T. M., Nemitz, E. G., Wood, C. R., Gallagher, M. W., Davies, F., O'Connor, E., and Harrison, R. M.: Boundary layer dynamics over London, UK, as observed using Doppler lidar during REPARTEE-II, Atmos. Chem. Phys., 11, 2111–2125, https://doi.org/10.5194/acp-11-2111-2011, 2011.

Bou-Zeid, E., Anderson, W., Katul, G. G., and Mahrt, L.: The persistent challenge of surface heterogeneity in boundary-layer meteorology: a review, Bound.-Lay. Meteorol., 177, 227–245, https://doi.org/10.1007/s10546-020-00551-8, 2020.

https://doi.org/10.5194/egusphere-2026-4121
Preprint. Discussion started: 5 August 2026

Brooks, I. M.: Finding boundary layer top: application of a wavelet covariance transform to lidar backscatter profiles, J. Atmos. Ocean. Tech., 20, 1092–1105, https://doi.org/10.1175/1520-0426(2003)020<1092:FBLTAO>2.0.CO;2, 2003.

Collaud Coen, M., Praz, C., Haefele, A., Ruffieux, D., Kaufmann, P., and Calpini, B.: Determination and climatology of the planetary boundary layer height above the Swiss plateau by in situ and remote sensing measurements as well as by the COSMO-2 model, Atmos. Chem. Phys., 14, 13205–13221, https://doi.org/10.5194/acp-14-13205-2014, 2014.

Du, C., Liu, S., Yu, X., Li, X., Chen, C., Peng, Y., Dong, Y., Dong, Z., and Wang, F.: Urban boundary layer height characteristics and relationship with particulate matter mass concentrations in Xi'an, central China, Aerosol Air Qual. Res., 13, 1598–1607, https://doi.org/10.4209/aaqr.2012.10.0274, 2013.

Emeis, S., Schäfer, K., and Münkel, C.: Surface-based remote sensing of the mixing-layer height: a review, Meteorol. Z., 17, 621–630, https://doi.org/10.1127/0941-2948/2008/0312, 2008.

Haeffelin, M., Angelini, F., Morille, Y., Martucci, G., Frey, S., Gobbi, G. P., Lolli, S., O'Dowd, C. D., Sauvage, L., Xueref-Rémy, I., Wastine, B., and Feist, D. G.: Evaluation of mixing-height retrievals from automatic profiling lidars and ceilometers in view of future integrated networks in Europe, Bound.-Lay. Meteorol., 143, 49–75, https://doi.org/10.1007/s10546-011-9643-z, 2012.

Jiang, Y., Xin, J., Wang, Y., Tang, G., Zhao, Y., Jia, D., Zhao, D., Wang, M., Dai, L., Wang, L., Wen, T., and Wu, F.: The thermodynamic structures of the planetary boundary layer dominated by synoptic circulations and the regular effect on air pollution in Beijing, Atmos. Chem. Phys., 21, 6111–6128, https://doi.org/10.5194/acp-21-6111-2021, 2021a.

Jiang, Y., Xin, J., Zhao, D., Jia, D., Tang, G., Quan, J., Wang, M., and Dai, L.: Analysis of differences between thermodynamic and material boundary layer structure: comparison of detection by ceilometer and microwave radiometer, Atmos. Res., 248, 105179, https://doi.org/10.1016/j.atmosres.2020.105179, 2021b.

Jin, Y., Kai, K., Kawai, K., Nagai, T., Sakai, T., Yamazaki, A., Uchiyama, A., Batdorj, D., Sugimoto, N., and Nishizawa, T.: Ceilometer calibration for retrieval of aerosol optical properties, J. Quant. Spectrosc. Ra., 153, 49–56, https://doi.org/10.1016/j.jqsrt.2014.10.009, 2015.

Knepp, T. N., Szykman, J. J., Long, R., Duvall, R. M., Krug, J., Beaver, M., Cavender, K., Kronmiller, K., Wheeler, M., Delgado, R., Hoff, R., Berkoff, T., Olson, E., Clark, R., Wolfe, D., Van Gilst, D., and Neil, D.: Assessment of mixed-layer height estimation from single-wavelength ceilometer profiles, Atmos. Meas. Tech., 10, 3963–3983, https://doi.org/10.5194/amt-10-3963-2017, 2017.

Kotthaus, S., Bravo-Aranda, J. A., Collaud Coen, M., Guerrero-Rascado, J. L., Costa, M. J., Cimini, D., O'Connor, E. J., Hervo, M., Alados-Arboledas, L., Jiménez-Portaz, M., Mona, L., Ruffieux, D., Illingworth, A., and Haeffelin, M.: Atmospheric boundary layer height from ground-based remote sensing: a review of capabilities and limitations, Atmos. Meas. Tech., 16, 433–479, https://doi.org/10.5194/amt-16-433-2023, 2023.

LeMone, M. A., Angevine, W. M., Bretherton, C. S., Chen, F., Dudhia, J., Fedorovich, E., Katsaros, K. B., Lenschow, D. H., Mahrt, L., Patton, E. G., Sun, J., Tjernström, M., and Weil, J.: 100 years of progress in boundary layer meteorology, Meteorol. Monogr., 59, 9.1–9.85, https://doi.org/10.1175/AMSMONOGRAPHS-D-18-0013.1, 2019.

https://doi.org/10.5194/egusphere-2026-4121
Preprint. Discussion started: 5 August 2026

Liu, S. and Liang, X.-Z.: Observed diurnal cycle climatology of planetary boundary layer height, J. Climate, 23, 5790–5809, https://doi.org/10.1175/2010JCLI3552.1, 2010.

Lu, H., Xie, M., Zhuang, B., Ma, D., Liu, B., Zhan, Y., Wang, T., Li, S., Li, M., and Zhu, K.: Impacts of atmospheric circulation patterns and cloud inhibition on aerosol radiative effect and boundary layer structure during winter air pollution in Sichuan Basin, China, Atmos. Chem. Phys., 24, 8963–8982, https://doi.org/10.5194/acp-24-8963-2024, 2024.

Ma, Y., Xin, J., Tian, Y., Yue, C., Zhou, X., Ren, Y., Hao, F., Wang, P., Xie, F., Ren, X., Zhao, D., Wu, L., Pan, X., and Wang, Z.: The interactions of aerosol and planetary boundary layer over a large city in the Mongolian Plateau, Sci. Total Environ., 907, 167985, https://doi.org/10.1016/j.scitotenv.2023.167985, 2024.

Mues, A., Rupakheti, M., Münkel, C., Lauer, A., Bozem, H., Hoor, P., Butler, T., and Lawrence, M. G.: Investigation of the mixing layer height derived from ceilometer measurements in the Kathmandu Valley and implications for local air quality, Atmos. Chem. Phys., 17, 8157–8176, https://doi.org/10.5194/acp-17-8157-2017, 2017.

Münkel, C., Eresmaa, N., Räsänen, J., and Karppinen, A.: Retrieval of mixing height and dust concentration with lidar ceilometer, Bound.-Lay. Meteorol., 124, 117–128, https://doi.org/10.1007/s10546-006-9103-3, 2007.

Oke, T. R., Mills, G., Christen, A., and Voogt, J. A.: Urban climates, Cambridge University Press, Cambridge, UK, https://doi.org/10.1017/9781139016476, 2017.

Pal, S., Haeffelin, M., and Batchvarova, E.: Exploring a geophysical process-based attribution technique for the determination of the atmospheric boundary layer depth using aerosol lidar and near-surface meteorological measurements, J. Geophys. Res.-Atmos., 118, 9277–9295, https://doi.org/10.1002/jgrd.50710, 2013.

Schween, J. H., Hirsikko, A., Löhnert, U., and Crewell, S.: Mixing-layer height retrieval with ceilometer and Doppler lidar: from case studies to long-term assessment, Atmos. Meas. Tech., 7, 3685–3704, https://doi.org/10.5194/amt-7-3685-2014, 2014.

Seidel, D. J., Ao, C. O., and Li, K.: Estimating climatological planetary boundary layer heights from radiosonde observations: comparison of methods and uncertainty analysis, J. Geophys. Res.-Atmos., 115, D16113, https://doi.org/10.1029/2009JD013680, 2010.

Shi, Y., Hu, F., Xiao, Z., Fan, G., and Zhang, Z.: Comparison of four different types of planetary boundary layer heights during a haze episode in Beijing, Sci. Total Environ., 711, 134928, https://doi.org/10.1016/j.scitotenv.2019.134928, 2020.

Sicard, M., Pérez, C., Rocadenbosch, F., Baldasano, J. M., and García-Vizcaino, D.: Mixed-layer depth determination in the Barcelona coastal area from regular lidar measurements: methods, results and limitations, Bound.-Lay. Meteorol., 119, 135–157, https://doi.org/10.1007/s10546-005-9005-9, 2006.

Strawbridge, K. B. and Snyder, B. J.: Planetary boundary layer height determination during Pacific 2001 using the advantage of a scanning lidar instrument, Atmos. Environ., 38, 5861–5871, https://doi.org/10.1016/j.atmosenv.2003.10.065, 2004.

Steyn, D. G., Baldi, M., and Hoff, R. M.: The detection of mixed layer depth and entrainment zone thickness from lidar backscatter profiles, J. Atmos. Ocean. Tech., 16, 953–959, https://doi.org/10.1175/1520-0426(1999)016<0953:TDOMLD>2.0.CO;2, 1999.

https://doi.org/10.5194/egusphere-2026-4121
Preprint. Discussion started: 5 August 2026

Stull, R. B.: An introduction to boundary layer meteorology, Kluwer Academic Publishers, Dordrecht, the Netherlands, https://doi.org/10.1007/978-94-009-3027-8, 1988.

Su, L., Xia, H., Yuan, J., Wang, Y., Maituerdi, A., and He, Q.: Study on daytime atmospheric mixing layer height based on 2-year coherent Doppler wind lidar observations at the southern edge of the Taklimakan Desert, Remote Sens., 16, 3005, https://doi.org/10.3390/rs16163005, 2024.

Sun, Z., Zhao, X., Li, Z., Tang, G., and Miao, S.: Boundary layer structure characteristics under objective classification of persistent pollution weather types in the Beijing area, Atmos. Chem. Phys., 21, 8863–8882, https://doi.org/10.5194/acp-21-8863-2021, 2021.

Tang, G., Zhang, J., Zhu, X., Song, T., Münkel, C., Hu, B., Schäfer, K., Liu, Z., Zhang, J., Wang, L., Xin, J., Suppan, P., and Wang, Y.: Mixing layer height and its implications for air pollution over Beijing, China, Atmos. Chem. Phys., 16, 2459–2475, https://doi.org/10.5194/acp-16-2459-2016, 2016.

Tucker, S. C., Senff, C. J., Weickmann, A. M., Brewer, W. A., Banta, R. M., Sandberg, S. P., Law, D. C., and Hardesty, R. M.: Doppler lidar estimation of mixing height using turbulence, shear, and aerosol profiles, J. Atmos. Ocean. Tech., 26, 673–688, https://doi.org/10.1175/2008JTECHA1157.1, 2009.

Vu, T. V., Shi, Z., Cheng, J., Zhang, Q., He, K., Wang, S., and Harrison, R. M.: Assessing the impact of clean air action on air quality trends in Beijing using a machine learning technique, Atmos. Chem. Phys., 19, 11303–11314, https://doi.org/10.5194/acp-19-11303-2019, 2019.

Wang, H., Li, Z., Lv, Y., Zhang, Y., Xu, H., Guo, J., and Goloub, P.: Determination and climatology of the diurnal cycle of the atmospheric mixing layer height over Beijing 2013–2018: lidar measurements and implications for air pollution, Atmos. Chem. Phys., 20, 8839–8854, https://doi.org/10.5194/acp-20-8839-2020, 2020.

Wang, M., Tang, G., Liu, Y., Ma, M., Yu, M., Hu, B., Zhang, Y., Wang, Y., and Wang, Y.: The difference in the boundary layer height between urban and suburban areas in Beijing and its implications for air pollution, Atmos. Environ., 260, 118552, https://doi.org/10.1016/j.atmosenv.2021.118552, 2021.

Wang, X., Zhang, R., Tan, Y., and Yu, W.: Dominant synoptic patterns associated with the decay process of PM2.5 pollution episodes around Beijing, Atmos. Chem. Phys., 21, 2491–2508, https://doi.org/10.5194/acp-21-2491-2021, 2021.

Wang, Y., Ma, Y., Yan, C., Yao, L., Cai, R., Li, S., Lin, Z., Zhao, X., Yin, R., Deng, C., Kangasluoma, J., He, X.-C., Hakala, S., Fan, X., Chen, S., Ma, Q., Kerminen, V.-M., Petäjä, T., Xin, J., Wang, L., Liu, B., Wang, W., Ge, M., Jiang, J., Liu, Y., Bianchi, F., Chu, B., Donahue, N. M., Martin, S. T., He, H., and Kulmala, M.: Sulfur dioxide transported from the residual layer drives atmospheric nucleation during haze periods in Beijing, Geophys. Res. Lett., 50, e2022GL100514, https://doi.org/10.1029/2022GL100514, 2023.

Xian, J., Luo, H., Lu, C., Lin, X., Yang, H., and Zhang, N.: Characteristics of the atmospheric boundary layer height: a perspective on turbulent motion, Sci. Total Environ., 919, 170895, https://doi.org/10.1016/j.scitotenv.2024.170895, 2024.

https://doi.org/10.5194/egusphere-2026-4121
Preprint. Discussion started: 5 August 2026

Xin, J., Ren, X., Ma, Y., Zhao, D., Wang, Y., Ye, J., Wang, Z., Cao, J., Vilà-Guerau de Arellano, J., and Martin, S. T.: Industrial dry heat island and dispersion of air pollutants induced by large coal-fired activities, Environ. Sci. Technol., 59, 2119–2130, https://doi.org/10.1021/acs.est.4c02300, 2025.

Yan, Y., Cai, X., Huang, Q., Qi, P., Song, Y., Zhang, H., and Zeng, L.: Long-term planetary boundary layer features and associated PM2.5 pollution anomalies in Beijing during the past 40 years, Theor. Appl. Climatol., 151, 1787–1804, https://doi.org/10.1007/s00704-023-04356-w, 2023.

Yang, S., Ma, Y., Zhang, W., Lin, Z., Lu, Z., Zhou, X., Ren, Y., Ren, X., Peng, K., Tan, Y., Wei, Y., Ahmad, M., Zhao, D., Kong, L., Ma, Y., Tian, Y., and Xin, J.: The interaction of atmospheric boundary layer and PM pollution in Mongolian Plateau: implication for the threshold control strategy, Atmos. Res., 316, 107937, https://doi.org/10.1016/j.atmosres.2025.107937, 2025.

Yang, X., Zhao, C., Guo, J., and Wang, Y.: Intensification of aerosol pollution associated with its feedback with surface solar radiation and winds in Beijing, J. Geophys. Res.-Atmos., 121, 4093–4099, https://doi.org/10.1002/2015JD024645, 2016.

Yin, D., Song, Q., Guo, Y., Jiang, Y., Dong, Z., Zhao, B., Wang, S., Gao, D., Chang, X., Zheng, H., Li, S., Li, Y., and Liu, B.: Regional transport characteristics of PM2.5 pollution events in Beijing during 2018–2021, J. Environ. Sci., 152, 503–515, https://doi.org/10.1016/j.jes.2024.05.044, 2025.

Zhang, J. P., Zhu, T., Zhang, Q. H., Li, C. C., Shu, H. L., Ying, Y., Dai, Z. P., Wang, X., Liu, X. Y., Liang, A. M., Shen, H. X., and Yi, B. Q.: The impact of circulation patterns on regional transport pathways and air quality over Beijing and its surroundings, Atmos. Chem. Phys., 12, 5031–5053, https://doi.org/10.5194/acp-12-5031-2012, 2012.

Zhang, T., Che, H. Z., Gong, Z. Q., Wang, Y. Q., Wang, J. Z., Yang, Y. Q., Gui, K., and Guo, B.: The two-way feedback effect between aerosol pollution and planetary boundary layer structure on the explosive rise of PM2.5 after the "Ten Statements of Atmosphere" in Beijing, Sci. Total Environ., 709, 136259, https://doi.org/10.1016/j.scitotenv.2019.136259, 2020.

Zhang, W., Hai, S., Zhao, Y., Sheng, L., Zhou, Y., Wang, W., and Li, W.: Numerical modeling of regional transport of PM2.5 during a severe pollution event in the Beijing–Tianjin–Hebei region in November 2015, Atmos. Environ., 254, 118393, https://doi.org/10.1016/j.atmosenv.2021.118393, 2021.

Zhao, D., Liu, G., Xin, J., Quan, J., Wang, Y., Wang, X., Dai, L., Gao, W., Tang, G., Hu, B., Ma, Y., Wu, X., Wang, L., Liu, Z., and Wu, F.: Haze pollution under a high atmospheric oxidization capacity in summer in Beijing: insights into formation mechanism of atmospheric physicochemical processes, Atmos. Chem. Phys., 20, 4575–4592, https://doi.org/10.5194/acp-20-4575-2020, 2020.

Zhou, Y., Han, Y., Hu, Z., Zhou, Q., Liu, Y., Dong, L., and Xiao, P.: Characteristics of planetary boundary layer height (PBLH) over Shenzhen, China: retrieval methods and air pollution conditions, Remote Sens., 17, 3937, https://doi.org/10.3390/rs17243937, 2025.

Zhu, X., Tang, G., Guo, J., Hu, B., Song, T., Wang, L., Xin, J., Gao, W., Münkel, C., Schäfer, K., Li, X., and Wang, Y.: Mixing layer height on the North China Plain and meteorological evidence of serious air pollution in southern Hebei, Atmos. Chem. Phys., 18, 4897–4910, https://doi.org/10.5194/acp-18-4897-2018, 2018.